Beyond Endpoint Gains: A Weight-Delta Audit of Medical Specialization

Praphul Singh[†,‡,*] **Shanu Kumar**[‡,§] **Akshat Agarwal**[†,‡]

[†]Oracle Health AI · [‡]IIT Kanpur · [§]MBZUAI

[*]**Correspondence:** praphul.singh@oracle.com

Abstract

Specialist language models are usually understood through endpoint gains: the generalist scores lower, the specialist scores higher, and the difference is treated as evidence of specialization. This leaves the released update itself largely unexamined. We propose a paired weight-delta path audit and apply it to two public, aligned generalist-to-medical-specialist checkpoint pairs: Gemma-3-4B-IT→MedGemma-4B-IT and Qwen2.5-7B-Instruct→HuatuoGPT-o1-7B. In both pairs, the full decoder-side update strongly reconstructs measured medical benchmark movement (0.974 and 1.183 endpoint-normalized retention), making each decoder delta an appropriate substrate for the audit. Yet the movement is not cleanly localized. MLP is the strongest broad component family in both pairs, but mixed off-domain movements, 10-seed matched controls, and endpoint-anchored rollbacks prevent a unique coarse-family explanation. The audit therefore separates update-level reconstruction from component-level explanation. Its claims concern text-only multiple-choice benchmark movement, not clinical validation, repair, or circuit-level mechanism.

1 Introduction

Domain-specialized language models are usually presented through endpoint comparisons. A base checkpoint is evaluated, a specialist checkpoint is evaluated, and the score difference is taken as the evidence of specialization. For medicine, this endpoint view is especially common: public exam-style benchmarks provide a convenient way to summarize whether a medical model improves over its generalist ancestor (Singhal et al., 2023, 2025; Nori et al., 2023; Sellergren et al., 2026). But endpoint scores leave a basic question unanswered: what does the released update itself carry?

This question matters because specialization is not a single scalar. The same checkpoint update that improves a target-domain benchmark may also introduce off-domain gains, off-domain regressions, and broad internal changes that are not visible from the final score alone. Conversely, a component family that appears useful in isolation may simply contain a large fraction of the update, rather than uniquely explaining the behavior. Endpoint evaluation tells us that two models differ; it does not audit whether the released update is broad or localized, target-specific or mixed, or genuinely component-structured.

We study this problem using two public aligned generalist-to-medical-specialist pairs: Gemma-3-4B-IT→MedGemma-4B-IT (Team et al., 2025; Sellergren et al., 2026) and Qwen2.5-7B-Instruct→HuatuoGPT-o1-7B (Yang et al., 2024; Chen et al., 2024). The former is our primary detailed audit; the latter tests whether its central pattern survives a change in architecture and checkpoint lineage. Because corresponding decoder tensors are aligned within each pair, the released checkpoint difference can be treated as an auditable path through weight space. We use medicine because it is consequential and widely benchmarked, but our object is measured benchmark movement along released updates, not clinical reliability.

This path view turns an endpoint comparison into a sequence of audit questions. First, what changed in the released checkpoint? A descriptive ΔW screen shows that the primary update is broad and structured across decoder layers and projection families, rather than a tiny localized edit. Second,

Findings of the Association for Computational Linguistics: EMNLP 2026, pages 25360–25378
October 24-29, 2026 ©2026 Association for Computational Linguistics

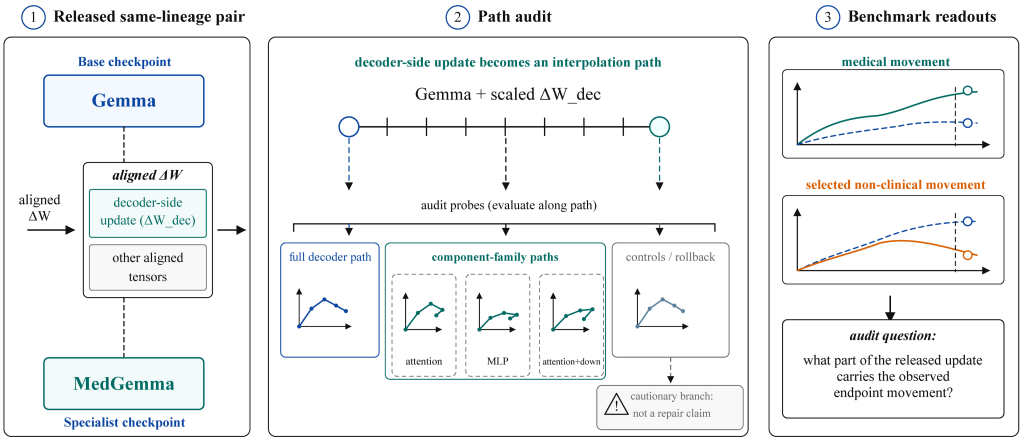

Figure 1: Paired checkpoint audit protocol, illustrated with the primary Gemma→MedGemma pair. For each aligned release, we first test whether the full decoder-side path reconstructs measured benchmark movement, then whether component-family interpretations survive matched controls and endpoint rollback.

does the observed decoder update actually reconstruct the measured medical gain? Evaluating the full decoder-side path shows that it does in both pairs. Third, what else moves along the same path? Selected non-clinical regressions and selected non-clinical gains coexist, while aggregate non-clinical accuracy is nearly flat, so the update is not well summarized as broad forgetting.

The final question is whether this movement has a simple component-level explanation. We test scoped component-family paths, matched random controls, and endpoint-anchored rollbacks. These probes show partial sufficiency but not clean localization. The MLP-family path is strongest among the tested scoped buckets, but it is also large; matched random controls can approach or exceed structured buckets; and rolling back individual families from the specialist endpoint trades medical retention against selected-regression recovery without revealing a clean knob. Thus the main component result is negative: the medical benchmark movement is path-reproducible, but not uniquely localized to a tested coarse component family.

This framing differs from task-vector transfer, model merging, model editing, and circuit discovery. Those lines of work often ask how to compose, optimize, repair, or mechanistically explain model behavior. We ask a narrower audit question: given an aligned specialist release, what benchmark movement is carried by its observed update, and how far do simple component explanations survive controls? The evidential order matters: endpoint movement motivates full-update reconstruction; reconstruction enables component partial-sufficiency tests; matched controls test distinctiveness; and rollback tests intervention utility. None of these stages alone supplies a circuit-level mechanism.

In this paper, we formulate a paired weight-delta path audit and evaluate it on two aligned medical-specialist releases. The audit uses a medical multiple-choice composite, a broader non-clinical suite, selected regression and gain diagnostics, and decoder-side path sweeps. It contributes a reusable protocol, a two-pair reconstruction result showing that measured medical movement is carried by each released decoder update, and a negative localization lesson: component claims must survive size/update-mass controls and endpoint rollback before becoming explanations.

2 Related Work

Medical language models and endpoint evaluation. Medical language models are commonly evaluated with public exam-style benchmarks, including MedQA and medical MMLU subsets (Jin et al., 2021; Hendrycks et al., 2021). Specialist systems and medical model releases report gains on these benchmarks through prompting, post-training, or domain-specific checkpoints (Singhal et al., 2023, 2025; Nori et al., 2023; Chen et al., 2023; Sellergren et al., 2026). Such results are useful behavioral summaries, but they are endpoint summaries: they do not show how the update that produced the gain is organized, nor do they establish reasoning quality or readiness for clinical deployment (Zhou et al., 2025; Ren et al., 2026). Our work is complementary: we use an auditable medical multiple-choice composite as a controlled

readout for studying the released specialization update itself.

Mechanistic localization and intervention analysis. Interpretability work studies where model behaviors are implemented, including feed-forward memories, knowledge neurons, attention heads, circuits, and sparse features (Petroni et al., 2019; Roberts et al., 2020; Geva et al., 2021; Dai et al., 2022; Geva et al., 2023; Elhage et al., 2021; Wang et al., 2023; Huben et al., 2024; Bricken et al., 2023; Marks et al., 2025). Causal mediation, causal tracing, attribution patching, and related interventions provide finer-grained evidence for particular prompts or mechanisms (Vig et al., 2020; Meng et al., 2022; Conmy et al., 2023; Syed et al., 2024; Hanna et al., 2024). Our component paths operate at a coarser granularity: they ask whether broad subsets of an observed update reproduce benchmark movement, not whether a minimal circuit or neuron set implements medical specialization. Prior work gives reasons to expect important MLP contributions, but a large family can look sufficient simply because it contains much of the update. We therefore treat an MLP result as a hypothesis to test against size- and energy-matched subsets, not as localization by itself.

Weight-space editing, interpolation, and merging. Weight-space methods modify or combine checkpoints through factual editing, model averaging, task arithmetic, and interference-aware merging (Meng et al., 2022, 2023; Wortsman et al., 2022; Matena and Raffel, 2022; Ilharco et al., 2023; Yadav et al., 2023; Song and Zheng, 2026). Activation- and representation-space interventions provide another control surface for steering behavior (Turner et al., 2024; Zou et al., 2025; Rimsky et al., 2024), and paired-model weight patching is especially close in spirit (Sun et al., 2026). These methods often treat deltas as objects to transfer, compose, optimize, edit, or causally explain. Our use of the delta is more modest: we treat the released same-lineage specialist update as evidence to audit, asking which benchmark movements appear along it and how far component explanations survive controls. In short, prior weight-delta work usually asks how to change or explain a model; we ask what a released specialist update can and cannot account for under benchmark readouts and negative controls.

Specialization tradeoffs and forgetting. Specialization and instruction tuning can improve target-domain behavior, while their effects on broader capabilities require separate evaluation (Bommasani et al., 2022; Sellergren et al., 2026; Ouyang et al., 2022). Continual-learning work often studies forgetting across a known training sequence; in our setting, only two released endpoints are observed. We therefore treat selected non-clinical regressions and gains as endpoint-conditioned diagnostics of this checkpoint pair, not as a complete estimate of forgetting or capability transfer.

3 Setup, Data, and Metrics

3.1 Paired Checkpoints

Our primary pair is Gemma-3-4B-IT and its medical-specialized descendant, MedGemma-4B-IT (Sellergren et al., 2026). We replicate the audit on Qwen2.5-7B-Instruct and HuatuoGPT-o1-7B (Yang et al., 2024; Chen et al., 2024). The analysis requires tensor alignment, not merely architectural similarity: corresponding decoder tensors must have matching shapes and parameter roles. This holds within each released pair. For Gemma, we define the observed checkpoint movement as

$$\Delta W_{\text{all}} = W_{\text{MedGemma}} - W_{\text{Gemma}},$$

and define the Qwen movement analogously. These are released checkpoint differences, not learned editors, adapters, or optimized merge directions. Both pairs are public, same-lineage, and tensor-aligned, so their updates can be audited without inferring a training trajectory or matching unrelated model families.

Because our benchmark inputs are text-only, the main interventions use the shared decoder-side portion of this movement. Let ΔW_{dec} denote the aligned decoder matrices from ΔW_{all}. The reference decoder path is

$$W_{\text{dec}}(t) = W_{\text{Gemma}} + t\Delta W_{\text{dec}}.$$

Here $t = 0$ is the base decoder and $t = 1$ is the decoder-side reconstruction of the specialist for text-only evaluation. MedGemma also contains multimodal components; we analyze encoder-side changes descriptively, but the primary behavioral audit targets the text-only decoder path. For Qwen, the same construction uses Qwen2.5 at $t = 0$ and

HuatuoGPT-o1 at $t = 1$. We use the linear additive path because it exposes fractions of the observed update and makes component masking and matched controls directly comparable. It is a diagnostic coordinate, not a claim about the training trajectory; curved paths such as SLERP remain useful robustness checks.

The Gemma decoder audit covers 238 aligned two-dimensional matrices containing 3.209B parameters (96.8% of the 3.316B aligned matrix parameters); 81 encoder-side matrices containing 0.107B parameters are described separately. The Qwen audit covers 196 aligned decoder projection matrices, approximately 6.53B non-embedding parameters. Embeddings, normalization parameters, and output heads are outside these matrix-family interventions.

3.2 Path Families

We evaluate three path families. The first is the full decoder path above, which serves as the reference reconstruction. It asks whether the observed decoder-side update carries the measured benchmark movement.

The second is a scoped-from-base component path. For a selected decoder family or bucket S, we apply only that subset of the update:

$$W_S(t) = W_{\text{Gemma}} + t\Delta W_S,$$

where $\Delta W_S \subseteq \Delta W_{\text{dec}}$. These paths test partial sufficiency: whether a subset alone can reproduce the reference movement.

The third is an endpoint-anchored rollback path. Starting from the full decoder update, we roll back only a selected family S:

$$W_{\text{anch},S}(\alpha) = W_{\text{dec}}(1) - (1-\alpha)\Delta W_S.$$

We run this sweep for attention and MLP with $\alpha \in \{0, 0.25, 0.5, 0.75, 1\}$. Thus $\alpha = 1$ is the full decoder update, while smaller values move only the selected family back toward Gemma. Scoped paths ask whether a family is sufficient by itself; anchored rollback asks what changes when that family is removed from an otherwise complete specialist update. Neither path is a minimal-circuit claim.

3.3 Evaluation Views

For both checkpoint pairs, the target-domain readout is the same 1,810-example public medical multiple-choice composite from MedQA and medical MMLU subsets. We restrict the composite to rows with auditable public gold labels compatible with a single scoring pipeline. The paper therefore audits measured benchmark movement, not clinical reliability.

View	Sources	Count
Medical composite	MedQA; MMLU Clinical Knowledge; MMLU Professional Medicine	1,810
Full non-clinical	GPQA Diamond; MMLU-Pro; CommonsenseQA; TruthfulQA MC1; Kaleidoscope text-only	7,325
Selected regressions	Endpoint drops with at least 80 examples and gap at least 0.02	2,469
Selected gains	Endpoint gains with at least 80 examples and gap at least 0.02	2,606

Table 1: Evaluation views. The medical composite is the target-domain readout; the full non-clinical suite checks aggregate endpoint behavior; selected regression and gain slices are conditional diagnostics used for path analysis.

Endpoint comparison	Δ	95% CI
Medical composite	+0.085	[+0.062, +0.108]
Selected-regression slices	-0.035	[-0.058, -0.015]
Selected-gain slices	+0.063	[+0.032, +0.084]

Table 2: Endpoint movements used to normalize the path readouts. Deltas are MedGemma minus Gemma.

We pair this with the same public non-clinical suite of 7,325 variable-choice multiple-choice examples from GPQA Diamond, MMLU-Pro, CommonsenseQA, TruthfulQA MC1, and text-only Kaleidoscope. This suite is used first as an aggregate endpoint check. MedGemma is slightly higher than Gemma overall on the aggregate suite (+0.0086 accuracy), so we do not claim broad non-clinical forgetting.

For path diagnostics, we also define selected non-clinical regression and gain slices. Regression slices are sources with at least 80 examples and a MedGemma–Gemma endpoint drop of at least 0.02 accuracy, yielding 2,469 examples. Gain slices are defined symmetrically, yielding 2,606 examples. These slices are endpoint-conditioned diagnostics of this checkpoint pair, not population-level estimates of all non-clinical behavior.

3.4 Normalized Readouts

Each example is scored by presenting the question and candidate options and choosing the option label

with the highest model score under a fixed prompt format. Medical examples have four options; the non-clinical suite supports variable option counts. The primary metric is accuracy.

For any metric m, let $m_G = m(W_{\text{Gemma}})$ and $m_M = m(W_{\text{MedGemma}})$. Medical retention is

$$\text{Ret}(W) = \frac{m(W) - m_G}{m_M - m_G}.$$

A value of 0 means no gain over Gemma, 1 means the full MedGemma endpoint gain, and values above 1 can occur when a path point slightly exceeds the specialist endpoint on the finite benchmark.

For a selected regression slice s, recovery is

$$\text{Rec}_s(W) = \frac{m_s(W) - m_{s,M}}{m_{s,G} - m_{s,M}},$$

where $m_{s,G} > m_{s,M}$ by construction. A value of 1 matches Gemma on the selected regressions, 0 matches MedGemma, and negative values are worse than the specialist endpoint. We report the macro-average over selected regression slices.

For selected gain slices, the analogous quantity measures how much of MedGemma's endpoint gain has been acquired:

$$\text{Gain}_s(W) = \frac{m_s(W) - m_{s,G}}{m_{s,M} - m_{s,G}}.$$

We macro-average this quantity across selected gain slices and keep it separate from regression recovery because the endpoint directions are opposite.

Confidence intervals use 2,000 paired bootstrap resamples with seed 1729. Medical metrics resample examples. Slice diagnostics resample examples within the endpoint-selected diagnostic set; slice definitions remain fixed after endpoint selection. The prompt, option-scoring rule, bootstrap procedure, path grid, and control construction are held fixed across pairs. Regression and gain slices are defined separately within each pair because they are endpoint-conditioned by design.

4 What Changed in the Released Update?

Before evaluating behavior, we first inspect the released checkpoint difference as a tensor object. For each aligned matrix, we compute $\Delta W_i = W_i^M - W_i^G$ and summarize its Frobenius norm, relative change $\|\Delta W_i\|_F / \|W_i^G\|_F$, root-mean-square

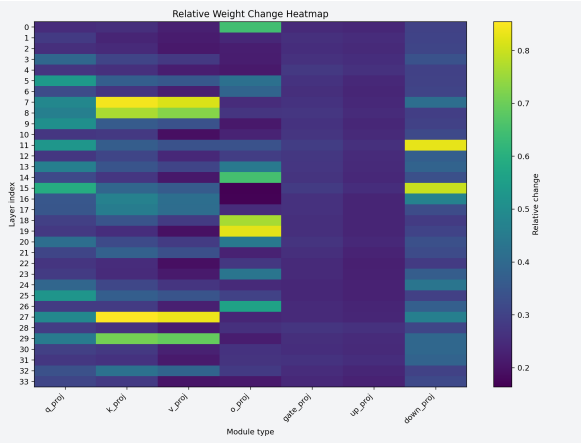

(a) Layer–module relative change

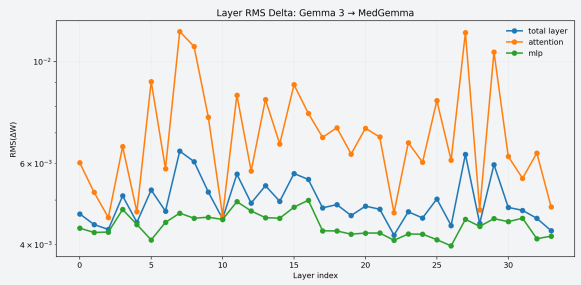

(b) Layerwise RMS change

Figure 2: Decoder-side ΔW screen. The released update is structured across layers and projection families rather than concentrated in a single obvious component. This screen motivates the tested buckets; behavioral claims come from path sweeps and controls.

change, and singular-value spectrum. These quantities are descriptive: they identify where the released update is large or structured, but they do not establish that a component causes benchmark behavior.

Across 884 shared state-dict keys, we find 319 aligned weight matrices: 238 in the shared decoder and 81 in encoder-side multimodal components, with no alignment failures. Because all benchmark inputs in this paper are text-only, the behavioral interventions target the shared decoder. Encoder-side changes are reported descriptively in the appendix.

The screen reveals a broad, structured update rather than a tiny localized edit. The appendix tables make this pattern concrete: decoder attention projections show the clearest relative-change hotspots, while MLP projections account for a large share of decoder-side update energy. Within the MLP family, `down_proj` is the most prominent projection by relative change, which motivates the mixed attention-plus-`down_proj` diagnostic. Spectral summaries give the same caution from a different angle: update energy is not concentrated in a

handful of singular directions, and effective ranks remain high across many decoder matrices (Appendix A.6). These facts make simple one-family explanations suspect before any behavioral evaluation is run.

The replication pair shows the same broad geometry at a larger scale. Its 196 aligned decoder projections comprise 112 attention and 84 MLP matrices. MLP accounts for 87.4% of projection parameters and 87.8% of update energy, while attention accounts for 12.6% and 12.2%, respectively. Mean effective ranks are 477.7 for attention and 1522.3 for MLP; within MLP, gate, up, and down projections all remain high-rank (1471, 1354, and 1742). Thus the MLP-heavy screen is a prior for intervention, not evidence that MLP uniquely carries the behavior.

This screen determines the probes used in the rest of the paper. The full decoder path keeps all aligned decoder matrices and serves as the reference reconstruction. The component paths test attention, MLP, a mixed attention-plus-`down_proj` bucket, and leave-one-family-out variants. Matched random controls then ask whether bucket behavior reflects component identity or simply the amount of update included. Anchored rollbacks ask the complementary endpoint question: what happens if one family is removed from an otherwise complete specialist update?

Thus the ΔW screen is a routing step. It shows that the released specialization update is broad enough to make simple localization suspect, but it does not by itself explain behavior. The next section tests whether the observed decoder update actually reconstructs benchmark movement.

5 Does the Decoder Path Reconstruct Benchmark Movement?

We next ask whether the observed decoder-side update is behaviorally meaningful for the text-only benchmarks. The full decoder path is

$$W_{\mathrm{dec}}(t) = W_{\mathrm{Gemma}} + t\Delta W_{\mathrm{dec}}.$$

This experiment is the reference reconstruction for the audit. The endpoint $t = 1$ checks whether the aligned decoder update accounts for the measured text-only endpoint movement; the trajectory between endpoints shows how medical and selected non-clinical behavior enter as the released update is introduced.

The full decoder path strongly reconstructs the measured medical benchmark movement. At the specialist endpoint, it reaches 0.974 normalized medical retention relative to the standalone Gemma→MedGemma medical gain (Table 2). This establishes the aligned decoder update as the relevant substrate for the text-only audit. Component probes are meaningful only because this audited decoder delta first recovers the endpoint behavior. We do not interpret this as a clinical result or as a mechanism; it is the coordinate system against which the component and control experiments are compared.

The trajectory reveals structure that the endpoint score hides. Medical retention rises early and remains high through the later part of the path; for example, the 0.50 point retains 0.863 of the medical gain while preserving 0.744 selected-regression recovery, and the 0.60 point retains 0.869 medical retention with 0.793 selected-gain acquisition. The bootstrap bands in Appendix Figure 7 support the qualitative medical trend, while also showing that selected regression and gain diagnostics are wider and should be read directionally. This does not imply broad forgetting: on the full non-clinical suite, MedGemma is slightly higher than Gemma overall (+0.0086 accuracy; 95% CI [-0.002, +0.020]). The selected-regression view is therefore a post-hoc diagnostic of slices that moved downward at the endpoint, not a global estimate of non-clinical capability.

The replication yields the same central result despite a different trajectory. The Qwen decoder path reaches 1.183 normalized medical retention at $t = 1$ (95% CI [0.962, 1.547]); values above 1 mean that this decoder reconstruction slightly exceeds the finite-sample specialist endpoint, not "118.3% capability." Medical retention rises from 0.866 at $t = 0.5$ to 1.085 at $t = 0.8$, while selected-regression recovery falls from 0.789 to 0.458 and selected-gain acquisition rises from 0.824 to 1.103. The Qwen endpoint movements are +0.0453 medical accuracy (95% CI [0.0254, 0.0641]), -0.0617 on its selected regressions, and +0.0554 on its selected gains.

The selected-gain view completes the picture. Some non-clinical slices improve rather than regress, and their gain acquisition also rises along the decoder path. Across both pairs, the specialist update is not well described as a one-dimensional tradeoff between medical ability and general ability. It carries the target medical movement together with heterogeneous off-domain changes.

We next ask whether a smaller component family

Figure 3: Full decoder-side paths for both checkpoint pairs. Each observed update reconstructs the medical endpoint movement while carrying mixed selected off-domain movements. The Qwen curves connect only evaluated path points. Selected slices are endpoint-conditioned diagnostics, not estimates of broad non-clinical forgetting.

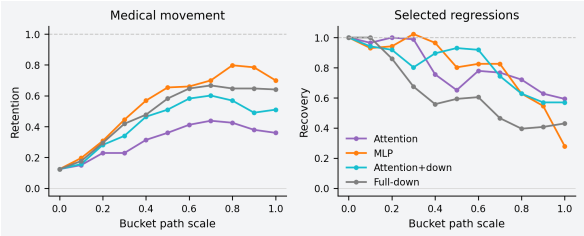

Figure 4: Scoped component-family paths show partial sufficiency, not localization. The MLP family is strongest among scoped buckets, but no tested bucket matches the full decoder path and the strongest bucket is also large.

explains the reconstructed movement, using scoped paths, matched controls, and anchored rollbacks.

6 Can Coarse Components Explain the Movement?

MLP is the strongest coarse bucket, but that alone does not establish localization. We therefore ask whether the reconstructed movement can be attributed to a smaller component family using three probes: scoped-from-base component paths, matched random controls, and endpoint-anchored rollbacks. These are coarse component-family diagnostics, not circuit-localization claims.

Scoped paths show partial sufficiency but not a complete explanation. The MLP path is strongest among the tested buckets, reaching 0.797 medical retention at its best point. Attention alone is weaker, and the attention-plus-down_proj bucket reaches 0.601 retention. The full-minus-down_proj path retains more medical movement than the mixed attention-plus-down_proj bucket, so down_proj is not necessary in isolation. The scoped-path result

Bucket	Best scale	Med. ret.	Reg. rec.
Attention	0.70	0.438	0.767
MLP	0.80	0.797	0.628
Attention+down	0.70	0.601	0.744
Full-down	0.70	0.667	0.465

Table 3: Best observed points for scoped decoder-side component-family paths. Medical retention is normalized by the endpoint medical gain; selected-regression recovery is endpoint-conditioned.

Diagnostic	Point	Med. ret.	Reg. rec.
MLP scoped best	$t = 0.80$	0.797	0.628
MLP param. ctrl (10)	$t = 1.00$	0.814±0.067	0.236±0.175
MLP ΔE ctrl (10)	$t = 1.00$	0.563±0.100	0.262±0.242
Attn+down scoped best	$t = 0.70$	0.601	0.744
Attn+down matrix ctrl (10)	$t = 1.00$	0.703±0.112	0.388±0.159
Attn+down param. ctrl (10)	$t = 1.00$	0.417±0.086	0.585±0.166
Attention rollback	$\alpha = 0$	0.699	0.279
MLP rollback	$\alpha = 0$	0.359	0.593

Table 4: Controls and anchored rollbacks test whether component sufficiency becomes explanation. The table distinguishes scoped-best path points from controls at $t = 1$ and full rollbacks at $\alpha = 0$. Control entries are mean ± standard deviation over 10 seeds.

is therefore suggestive but limited: broad families can reproduce parts of the medical movement, but no tested bucket matches the full decoder path.

The strongest scoped result also raises an obvious concern: the MLP bucket is large. We therefore compare structured buckets with matched random controls that match matrix count, parameter count, or ΔW-energy. For each target and matching rule, we run 10 seeded draws. These controls are still coarse nulls, but they test whether a structured bucket is clearly distinguished from similarly sized or similarly energetic subsets of the same released update.

Diagnostic	Gemma–MedGemma	Qwen–Huatuo
Medical endpoint gain	+0.0845	+0.0453
Full decoder retention	0.974	1.183
MLP retention at $t = 1$	0.699	1.024
MLP parameter control	0.814	1.115
MLP ΔW-energy control	0.563	1.098
Attention rollback: med./reg.	0.699 / 0.279	0.756 / 0.387
MLP rollback: med./reg.	0.359 / 0.593	0.293 / 0.986

Table 5: Cross-pair audit summary. Control entries are mean medical retention at $t = 1$; rollback entries report medical retention / selected-regression recovery after fully removing the named family.

Matched controls weaken a unique-family interpretation: if random matched subsets approach a structured bucket, the bucket is not a unique semantic carrier at this granularity. At $t = 1$, parameter-count-matched MLP controls average 0.814 medical retention, exceeding the structured MLP value (0.699), although their selected-regression recovery remains close. For attention-plus-`down_proj`, matrix-count controls average higher medical retention than the structured bucket, while parameter-count controls approach its selected-regression recovery. These results do not imply that component identity is irrelevant, but they show that bucket performance depends substantially on how much of the observed update is included and on which axis is matched (Appendix Figure 9). Component-family paths are therefore partial sufficiency probes, not unique explanations.

The replication makes this control result harder to dismiss as pair-specific. For Qwen–HuatuoGPT, MLP reaches 1.024 medical retention at $t = 1$, but the MLP parameter- and energy-matched controls reach 1.115 and 1.098 on average. Attention reaches only 0.341, while attention-plus-`down_proj` reaches 0.841. These are comparisons at the same endpoint scale; we do not compare a bucket's best intermediate point against a control evaluated only at $t = 1$.

Endpoint-anchored rollbacks provide the complementary test. Instead of asking whether a family can reproduce movement from the base model, they ask what happens when one family is rolled back from an otherwise complete specialist update.

The rollback result again argues against a simple component knob. Full MLP rollback recovers more of the selected regressions than full attention rollback (0.593 versus 0.279), but it also costs far more medical retention (0.359 versus 0.699). Partial rollbacks do not produce a clean frontier where regressions are recovered while medical retention is preserved. Thus the endpoint behavior is not organized as a monotone sum of independently helpful component families. Qwen shows the same tradeoff more sharply: full MLP rollback retains 0.293 of the medical gain while recovering 0.986 of selected regressions, whereas attention rollback retains 0.756 medical and recovers 0.387. Neither pair offers a clean family-level repair that preserves the target gain while reversing the selected regressions.

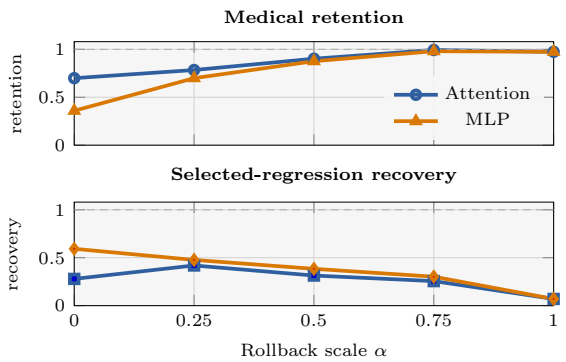

Figure 5: Endpoint-anchored rollback sweeps show that no family is a clean repair knob. MLP rollback recovers selected regressions more than attention rollback, but at a much larger medical-retention cost.

Taken together, these experiments make the component result mostly negative but useful. The medical benchmark movement is reproducible along the full decoder path, and broad families can reproduce parts of it. However, matched controls and anchored rollbacks prevent a stronger localization claim: at the tested granularity, no component family uniquely explains the movement.

Empirical summary. The main results are therefore threefold. First, the medical benchmark movement is carried by the observed decoder-side updates: both full paths reconstruct the measured medical gain. Second, each update carries heterogeneous off-domain movement, with selected regressions, selected gains, and a nearly flat aggregate non-clinical endpoint. Third, coarse component families are useful probes but weak explanations: MLP is the strongest scoped bucket, yet matched controls and anchored rollbacks prevent a unique family-level localization claim, and this negative conclusion replicates across both checkpoint pairs.

7 Discussion

Same-lineage specialist releases deserve an analysis layer between endpoint evaluation and circuit

discovery. Endpoint evaluation treats each specialist as a model; a weight-delta audit treats the aligned generalist-to-specialist difference as an object with internal structure. Across two medical checkpoint pairs, the full decoder update reconstructs the measured target movement, while selected off-domain gains and regressions travel differently along the path. This is stronger than an endpoint comparison but weaker than a mechanistic explanation: the paths establish an auditable substrate, not the features, circuits, training examples, or historical trajectory that caused it.

The cross-pair result also sharpens how component evidence should be read. MLP is the strongest broad component family in both pairs, consistent with the descriptive energy screen and prior work on feed-forward knowledge storage. Yet MLP is also the dominant parameter and update-energy family, and matched random subsets can equal or exceed it. The reproducible conclusion is therefore not "medical specialization is in the MLPs." It is that MLP provides a useful intervention prior whose apparent sufficiency does not survive controls as unique semantic localization. Parameter mass and update energy can masquerade as explanation.

Rollback makes the practical consequence visible. Removing MLP recovers more of the selected regressions in both pairs, but it also removes much more medical movement than attention rollback. No tested family is a clean repair knob. In practice, the audit is better suited to release comparison, regression triage, and prioritizing finer-grained follow-up than to editing a deployed model. A promising bucket should earn stronger evidence through controls, multiple checkpoint pairs, finer causal interventions, and open-ended behavioral tests.

Finally, the non-clinical views remain conditional diagnostics. Their source composition differs semantically, the gain/regression slices are selected from each pair's endpoints, and multiple-choice accuracy does not capture calibration or generation quality. A useful next step is to pair the weight-space audit with open-ended clinical tasks and blinded judge ensembles, explicitly measuring judge variance rather than replacing auditable labels with a single evaluator. The present result is deliberately narrower: for two released, tensor-aligned medical specializations, full-path reconstruction replicates, whereas a unique coarse-family explanation does not.

8 Conclusion

We audit two public generalist-to-medical-specialist weight deltas. In both Gemma–MedGemma and Qwen–HuatuoGPT, the aligned decoder path reconstructs the measured medical benchmark gain while carrying heterogeneous selected non-clinical movement. MLP is the strongest broad component family, but matched controls and endpoint-anchored rollbacks prevent unique localization: size and update energy explain substantial apparent sufficiency, and removing MLP trades regression recovery for medical retention. Endpoint gains should therefore be paired with update-level audits before component or repair narratives are inferred; these results are neither clinical validation nor circuit explanation.

9 Limitations

This study covers two public, tensor-aligned medical checkpoint pairs, not a general theory of post-training. Both audited intervention paths operate on decoder-only language-model backbones specialized for medicine; other architectures, domains, sizes, and training recipes may organize their updates differently, and the protocol requires comparable endpoint tensors. The evaluation is text-only and multiple-choice. It does not measure free-form clinical generation, calibration, abstention, multimodal use, robustness, harmful-answer behavior, or clinical utility. Public benchmark overlap may exist, so gains are measured benchmark movement rather than out-of-distribution medical generalization.

The additive weight path is a counterfactual audit coordinate, not the historical training trajectory or a deployment recommendation. Alternative geometries such as SLERP could yield different intermediate behavior. Embeddings, normalization parameters, output heads, and Gemma's vision-side parameters are outside the primary matrix-family interventions. Component buckets test coarse partial sufficiency rather than circuits, features, token-level mechanisms, or minimal subsets. Ten-seed matched controls for both pairs are informative but not exhaustive null distributions. Finally, regression and gain slices are selected separately from each pair's endpoints and combine semantically varied benchmarks; they are diagnostic views, not population estimates of general capability or forgetting.

Acknowledgments

We thank Sri Gadde, Krishnaram Kenthapadi, Raefer Gabriel, Anurag Dwarkanath, and Kiran Rama from the Oracle Health leadership team for their guidance, thoughtful feedback, and continued support throughout this work. We also gratefully acknowledge Oracle Health AI for supporting this research and providing the computational resources that enabled the experiments and analyses presented in this paper.

Ethics Statement

This work analyzes public checkpoints and public benchmark examples, and uses no patient records, protected health information, or human-subject data. The medical setting is sensitive: exam-style multiple-choice gains should not be read as clinical reliability, safe advice generation, calibrated uncertainty, or readiness for patient- or clinician-facing use. The interpolation, bucket, rollback, and neuron-diagnostic analyses are retrospective audit probes, not certification, repair, or deployment methods. Weight-space analysis can be dual-use because it may inform capability modification; we mitigate this by keeping claims benchmark-scoped, reporting negative controls and limitations with the positive results, not releasing modified checkpoints, and framing the contribution as audit evidence rather than clinical guidance.

References

Rishi Bommasani, Drew A. Hudson, Ehsan Adeli, Russ Altman, Simran Arora, Sydney von Arx, Michael S. Bernstein, Jeannette Bohg, Antoine Bosselut, Emma Brunskill, Erik Brynjolfsson, Shyamal Buch, Dallas Card, Rodrigo Castellon, Niladri Chatterji, Annie Chen, Kathleen Creel, Jared Quincy Davis, Dora Demszky, and 95 others. 2022. On the opportunities and risks of foundation models. *Preprint*, arXiv:2108.07258.

Trenton Bricken, Adly Templeton, Joshua Batson, Brian Chen, Adam Jermyn, Tom Conerly, Nick Turner, Cem Anil, Carson Denison, Amanda Askell, Robert Lasenby, Yifan Wu, Shauna Kravec, Nicholas Schiefer, Tim Maxwell, Nicholas Joseph, Zac Hatfield-Dodds, Alex Tamkin, Karina Nguyen, and 6 others. 2023. Towards monosemanticity: Decomposing language models with dictionary learning. *Transformer Circuits Thread*.

Junying Chen, Zhenyang Cai, Ke Ji, Xidong Wang, Wanlong Liu, Rongsheng Wang, Jianye Hou, and Benyou Wang. 2024. Huatuogpt-o1, towards medical complex reasoning with llms. *Preprint*, arXiv:2412.18925.

Zeming Chen, Alejandro Hernández Cano, Angelika Romanou, Antoine Bonnet, Kyle Matoba, Francesco Salvi, Matteo Pagliardini, Simin Fan, Andreas Köpf, Amirkeivan Mohtashami, Alexandre Sallinen, Alireza Sakhaeirad, Vinitra Swamy, Igor Krawczuk, Deniz Bayazit, Axel Marmet, Syrielle Montariol, Mary-Anne Hartley, Martin Jaggi, and Antoine Bosselut. 2023. Meditron-70b: Scaling medical pretraining for large language models. *Preprint*, arXiv:2311.16079.

Arthur Conmy, Augustine Mavor-Parker, Aengus Lynch, Stefan Heimersheim, and Adrià Garriga-Alonso. 2023. Towards automated circuit discovery for mechanistic interpretability. In *Advances in Neural Information Processing Systems*, volume 36, pages 16318–16352. Curran Associates, Inc.

Damai Dai, Li Dong, Yaru Hao, Zhifang Sui, Baobao Chang, and Furu Wei. 2022. Knowledge neurons in pretrained transformers. In *Proceedings of the 60th Annual Meeting of the Association for Computational Linguistics (Volume 1: Long Papers)*, pages 8493–8502, Dublin, Ireland. Association for Computational Linguistics.

Nelson Elhage, Neel Nanda, Catherine Olsson, Tom Henighan, Nicholas Joseph, Ben Mann, Amanda Askell, Yuntao Bai, Anna Chen, Tom Conerly, Nova DasSarma, Dawn Drain, Deep Ganguli, Zac Hatfield-Dodds, Danny Hernandez, Andy Jones, Jackson Kernion, Liane Lovitt, Kamal Ndousse, and 6 others. 2021. A mathematical framework for transformer circuits. *Transformer Circuits Thread*.

Mor Geva, Jasmijn Bastings, Katja Filippova, and Amir Globerson. 2023. Dissecting recall of factual associations in auto-regressive language models. In *Proceedings of the 2023 Conference on Empirical Methods in Natural Language Processing*, pages 12216–12235, Singapore. Association for Computational Linguistics.

Mor Geva, Roei Schuster, Jonathan Berant, and Omer Levy. 2021. Transformer feed-forward layers are key-value memories. In *Proceedings of the 2021 Conference on Empirical Methods in Natural Language Processing*, pages 5484–5495, Online and Punta Cana, Dominican Republic. Association for Computational Linguistics.

Michael Hanna, Sandro Pezzelle, and Yonatan Belinkov. 2024. Have faith in faithfulness: Going beyond circuit overlap when finding model mechanisms. *Preprint*, arXiv:2403.17806.

Dan Hendrycks, Collin Burns, Steven Basart, Andy Zou, Mantas Mazeika, Dawn Song, and Jacob Steinhardt. 2021. Measuring massive multitask language understanding. In *International Conference on Learning Representations*.

Robert Huben, Hoagy Cunningham, Logan Smith, Aidan Ewart, and Lee Sharkey. 2024. Sparse autoencoders find highly interpretable features in language models. In *The Twelfth International Conference on Learning Representations*.

Gabriel Ilharco, Marco Tulio Ribeiro, Mitchell Wortsman, Ludwig Schmidt, Hannaneh Hajishirzi, and Ali Farhadi. 2023. Editing models with task arithmetic. In *The Eleventh International Conference on Learning Representations*.

Di Jin, Eileen Pan, Nassim Oufattole, Wei-Hung Weng, Hanyi Fang, and Peter Szolovits. 2021. What disease does this patient have? a large-scale open domain question answering dataset from medical exams. *Applied Sciences*, 11(14):6421.

Samuel Marks, Can Rager, Eric J Michaud, Yonatan Belinkov, David Bau, and Aaron Mueller. 2025. Sparse feature circuits: Discovering and editing interpretable causal graphs in language models. In *The Thirteenth International Conference on Learning Representations*.

Michael S Matena and Colin Raffel. 2022. Merging models with fisher-weighted averaging. In *Advances in Neural Information Processing Systems*, volume 35, pages 17703–17716. Curran Associates, Inc.

Kevin Meng, David Bau, Alex Andonian, and Yonatan Belinkov. 2022. Locating and editing factual associations in gpt. In *Advances in Neural Information Processing Systems*, volume 35, pages 17359–17372. Curran Associates, Inc.

Kevin Meng, Arnab Sen Sharma, Alex J Andonian, Yonatan Belinkov, and David Bau. 2023. Mass-editing memory in a transformer. In *The Eleventh International Conference on Learning Representations*.

Harsha Nori, Nicholas King, Scott Mayer McKinney, Dean Carignan, and Eric Horvitz. 2023. Capabilities of gpt-4 on medical challenge problems. *Preprint*, arXiv:2303.13375.

Long Ouyang, Jeffrey Wu, Xu Jiang, Diogo Almeida, Carroll Wainwright, Pamela Mishkin, Chong Zhang, Sandhini Agarwal, Katarina Slama, Alex Ray, John Schulman, Jacob Hilton, Fraser Kelton, Luke Miller, Maddie Simens, Amanda Askell, Peter Welinder, Paul F Christiano, Jan Leike, and Ryan Lowe. 2022. Training language models to follow instructions with human feedback. In *Advances in Neural Information Processing Systems*, volume 35, pages 27730–27744. Curran Associates, Inc.

Fabio Petroni, Tim Rocktäschel, Sebastian Riedel, Patrick Lewis, Anton Bakhtin, Yuxiang Wu, and Alexander Miller. 2019. Language models as knowledge bases? In *Proceedings of the 2019 Conference on Empirical Methods in Natural Language Processing and the 9th International Joint Conference on Natural Language Processing (EMNLP-IJCNLP)*, pages 2463–2473, Hong Kong, China. Association for Computational Linguistics.

Xiaohan Ren, Chenxiao Fan, Wenyin Ma, Hongliang He, Chongming Gao, Xiaoyan Zhao, and Fuli Feng. 2026. Medical reasoning with large language models: A survey and mr-bench. *Preprint*, arXiv:2604.08559.

Nina Rimsky, Nick Gabrieli, Julian Schulz, Meg Tong, Evan Hubinger, and Alexander Turner. 2024. Steering llama 2 via contrastive activation addition. In *Proceedings of the 62nd Annual Meeting of the Association for Computational Linguistics (Volume 1: Long Papers)*, pages 15504–15522, Bangkok, Thailand. Association for Computational Linguistics.

Adam Roberts, Colin Raffel, and Noam Shazeer. 2020. How much knowledge can you pack into the parameters of a language model? In *Proceedings of the 2020 Conference on Empirical Methods in Natural Language Processing (EMNLP)*, pages 5418–5426, Online. Association for Computational Linguistics.

Andrew Sellergren, Sahar Kazemzadeh, Tiam Jaroensri, Atilla Kiraly, Madeleine Traverse, Timo Kohlberger, Shawn Xu, Fayaz Jamil, Cían Hughes, Charles Lau, Justin Chen, Fereshteh Mahvar, Liron Yatziv, Tiffany Chen, Bram Sterling, Stefanie Anna Baby, Susanna Maria Baby, Jeremy Lai, Samuel Schmidgall, and 62 others. 2026. Medgemma technical report. *Preprint*, arXiv:2507.05201.

Karan Singhal, Shekoofeh Azizi, Tao Tu, S. Sara Mahdavi, Jason Wei, Hyung Won Chung, Nathan Scales, Ajay Tanwani, Heather Cole-Lewis, Stephen Pfohl, Perry Payne, Martin Seneviratne, Paul Gamble, Chris Kelly, Abubakr Babiker, Nathanael Schärli, Aakanksha Chowdhery, Philip Mansfield, Dina Demner-Fushman, and 13 others. 2023. Large language models encode clinical knowledge. *Nature*, 620(7972):172–180.

Karan Singhal, Tao Tu, Juraj Gottweis, Rory Sayres, Ellery Wulczyn, Mohamed Amin, Le Hou, Kevin Clark, Stephen R. Pfohl, Heather Cole-Lewis, Darlene Neal, Qazi Mamunur Rashid, Mike Schaekermann, Amy Wang, Dev Dash, Jonathan H. Chen, Nigam H. Shah, Sami Lachgar, Philip Andrew Mansfield, and 16 others. 2025. Toward expert-level medical question answering with large language models. *Nature Medicine*, 31(3):943–950.

Mingyang Song and Mao Zheng. 2026. Model merging in the era of large language models: Methods, applications, and future directions. *Preprint*, arXiv:2603.09938.

Chenghao Sun, Chengsheng Zhang, Guanzheng Qin, Rui Dai, and Xinmei Tian. 2026. Weight patching: Toward source-level mechanistic localization in llms. *Preprint*, arXiv:2604.13694.

Aaquib Syed, Can Rager, and Arthur Conmy. 2024. Attribution patching outperforms automated circuit discovery. In *Proceedings of the 7th BlackboxNLP*

Workshop: Analyzing and Interpreting Neural Networks for NLP, pages 407–416, Miami, Florida, US. Association for Computational Linguistics.

Gemma Team, Aishwarya Kamath, Johan Ferret, Shreya Pathak, Nino Vieillard, Ramona Merhej, Sarah Perrin, Tatiana Matejovicova, Alexandre Ramé, Morgane Rivière, Louis Rouillard, Thomas Mesnard, Geoffrey Cideron, Jean-Bastien Grill, Sabela Ramos, Edouard Yvinec, Michelle Casbon, Etienne Pot, Ivo Penchev, and 196 others. 2025. Gemma 3 technical report. *Preprint*, arXiv:2503.19786.

Alexander Matt Turner, Lisa Thiergart, Gavin Leech, David Udell, Juan J. Vazquez, Ulisse Mini, and Monte MacDiarmid. 2024. Steering language models with activation engineering. *Preprint*, arXiv:2308.10248.

Jesse Vig, Sebastian Gehrmann, Yonatan Belinkov, Sharon Qian, Daniel Nevo, Yaron Singer, and Stuart Shieber. 2020. Investigating gender bias in language models using causal mediation analysis. In *Advances in Neural Information Processing Systems*, volume 33, pages 12388–12401. Curran Associates, Inc.

Kevin Ro Wang, Alexandre Variengien, Arthur Conmy, Buck Shlegeris, and Jacob Steinhardt. 2023. Interpretability in the wild: a circuit for indirect object identification in GPT-2 small. In *The Eleventh International Conference on Learning Representations*.

Mitchell Wortsman, Gabriel Ilharco, Samir Ya Gadre, Rebecca Roelofs, Raphael Gontijo-Lopes, Ari S Morcos, Hongseok Namkoong, Ali Farhadi, Yair Carmon, Simon Kornblith, and Ludwig Schmidt. 2022. Model soups: averaging weights of multiple fine-tuned models improves accuracy without increasing inference time. In *Proceedings of the 39th International Conference on Machine Learning*, volume 162 of *Proceedings of Machine Learning Research*, pages 23965–23998. PMLR.

Prateek Yadav, Derek Tam, Leshem Choshen, Colin Raffel, and Mohit Bansal. 2023. Ties-merging: Resolving interference when merging models. In *Advances in Neural Information Processing Systems*, volume 36, pages 7093–7115. Curran Associates, Inc.

An Yang, Baosong Yang, Beichen Zhang, Binyuan Hui, Bo Zheng, Bowen Yu, Chengyuan Li, Dayiheng Liu, Fei Huang, Haoran Wei, Huan Lin, Jian Yang, Jianhong Tu, Jianwei Zhang, Jianxin Yang, Jiaxi Yang, Jingren Zhou, Junyang Lin, Kai Dang, and 23 others. 2024. Qwen2.5 technical report. *Preprint*, arXiv:2412.15115.

Shuang Zhou, Wenya Xie, Jiaxi Li, Zaifu Zhan, Meijia Song, Han Yang, Cheyenna Espinoza, Lindsay Welton, Xinnie Mai, Yanwei Jin, Zidu Xu, Yuen-Hei Chung, Yiyun Xing, Meng-Han Tsai, Emma Schaffer, Yucheng Shi, Ninghao Liu, Zirui Liu, and Rui Zhang. 2025. Automating expert-level medical reasoning evaluation of large language models. *npj Digital Medicine*, 9(1):34.

Andy Zou, Long Phan, Sarah Chen, James Campbell, Phillip Guo, Richard Ren, Alexander Pan, Xuwang Yin, Mantas Mazeika, Ann-Kathrin Dombrowski, Shashwat Goel, Nathaniel Li, Michael J. Byun, Zifan Wang, Alex Mallen, Steven Basart, Sanmi Koyejo, Dawn Song, Matt Fredrikson, and 2 others. 2025. Representation engineering: A top-down approach to ai transparency. *Preprint*, arXiv:2310.01405.

A Additional Results and Diagnostics

A.1 Evaluation Details and Endpoint Movements

The primary medical composite contains only rows with auditable public labels compatible with the scoring protocol. The non-clinical suite and the selected regression/gain diagnostics follow the definitions in Section 3. Table 6 summarizes the evaluation views, and Table 7 reports the endpoint movements that define the normalized readouts.

View	Sources / rule	Count
Medical composite	MedQA; MMLU Clinical Knowledge; MMLU Professional Medicine	1,810
Full non-clinical	GPQA Diamond; MMLU-Pro; CommonsenseQA; TruthfulQA MC1; Kaleidoscope text-only	7,325
Selected regressions	Endpoint drops with at least 80 examples and gap at least 0.02	2,469
Selected gains	Endpoint gains with at least 80 examples and gap at least 0.02	2,606

Table 6: Evaluation views used in the audit. Selected regression and gain views are endpoint-conditioned diagnostics, not population estimates of all non-clinical behavior.

View	Δ	95% CI
Medical	+0.085	[+0.062, +0.108]
Selected regressions	-0.035	[-0.058, -0.015]
Selected gains	+0.063	[+0.032, +0.084]

Table 7: Endpoint movements used to normalize the path readouts. Deltas are MedGemma minus Gemma.

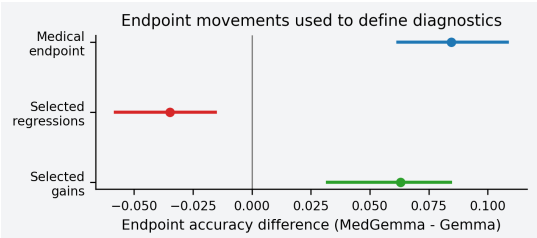

Figure 6: Endpoint movement summary with bootstrap intervals. The full non-clinical aggregate is used descriptively in the main text and is not the denominator for the selected-slice readouts.

Source	Count	Gemma	MedGemma	Δ	95% CI
MedQA (USMLE 4-option)	1,273	0.469	0.551	+0.082	[+0.053, +0.109]
MMLU Clinical Knowledge	265	0.604	0.645	+0.042	[-0.019, +0.098]
MMLU Professional Medicine	272	0.529	0.669	+0.140	[+0.081, +0.199]
Composite	1,810	0.498	0.582	+0.085	[+0.062, +0.108]

Table 8: Medical endpoint performance by source. This table makes explicit that the composite gain is positive across the three medical sources, while the composite is example-weighted and therefore MedQA-dominated.

View	Count	Gemma	MedGemma	Δ	95% CI
Full non-clinical	7,325	0.410	0.418	+0.009	[-0.002, +0.020]

Table 9: Full non-clinical endpoint aggregate. The small positive aggregate movement motivates treating selected regressions as diagnostics rather than broad forgetting.

All model evaluations use the same multiple-choice scoring rule: each example is presented with the question stem and answer options, and the predicted answer is the option label with the highest model score. Medical examples use four options; the non-clinical suite supports variable option counts. Bootstrap intervals use 2,000 paired resamples with seed 1729; medical metrics resample examples, while slice diagnostics resample examples within the fixed endpoint-selected sets.

A.2 Full Decoder-Side Path Diagnostics

Table 12 gives the full decoder-side path grid used for the main path analysis. Normalized retention is computed against the standalone endpoint evaluations in Table 7. A separately evaluated $t = 0$ reconstruction serves only as a consistency check and is omitted from the grid; it is not used as the normalization denominator. The selected-regression and selected-gain figures show that endpoint-conditioned slices move heterogeneously, which is why the paper reports regression recovery and gain acquisition as separate readouts.

t	Med. acc.	Med. ret.	Reg. rec.	Gain acq.
0.10	0.5193	0.255	0.953	0.220
0.20	0.5293	0.373	0.965	0.354
0.25	0.5365	0.458	1.047	0.445
0.30	0.5448	0.556	0.895	0.506
0.40	0.5619	0.758	0.849	0.610
0.50	0.5707	0.863	0.744	0.665
0.60	0.5713	0.869	0.581	0.793
0.70	0.5751	0.915	0.651	0.866
0.80	0.5773	0.941	0.488	0.902
0.90	0.5818	0.993	0.372	0.866
1.00	0.5801	0.974	0.070	0.841

Table 12: Full decoder-side path grid. Gain acquisition is the acquired fraction of selected endpoint gains; selected-regression recovery is computed on endpoint-regression slices.

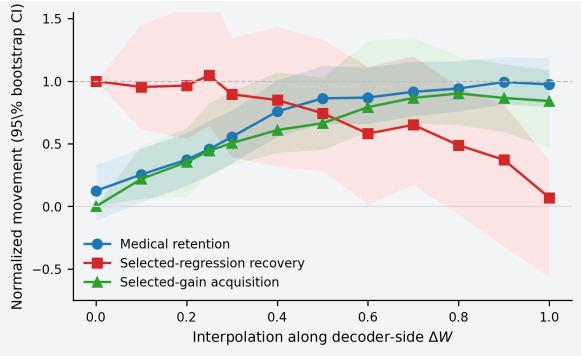

Figure 7: Bootstrap confidence bands for the Gemma–MedGemma full decoder path. Medical reconstruction is the most stable readout; selected-slice diagnostics have wider intervals and are interpreted directionally.

A.3 Component Buckets and Matched Controls

Table 14 reports the best observed point for each scoped component-family path, Table 15 reports 10 seeded matched controls under the same evaluation readouts, and Table 16 reports the anchored rollback sweeps used in Section 6. The controls are not exhaustive null distributions, but they make the size- and update-mass checks less dependent on a single random draw.

Bucket	Matrices	Param. %	ΔW energy %	Role
Full decoder	238	100.0	100.0	Reference
Attention family	136	16.7	35.0	Component
MLP family	102	83.3	65.0	Component
Attn+down	170	44.4	44.2	Mixed
Full–down	204	72.2	90.8	Leave-one-out

Table 13: Bucket definitions for decoder-side component-family sweeps. Shares are relative to the full decoder-side bucket.

Bucket	Scale	Med. ret. [CI]	Reg. rec. [CI]
Attention	0.70	0.438 [0.205, 0.673]	0.767 [-0.122, 1.276]
MLP	0.80	0.797 [0.608, 1.029]	0.628 [-0.154, 1.193]
Attention+down	0.70	0.601 [0.374, 0.849]	0.744 [0.020, 1.485]
Full-down	0.70	0.667 [0.454, 0.892]	0.465 [-0.286, 0.922]

Table 14: Best observed scoped component-family points with bootstrap intervals.

Source	Count	Gemma	MedGemma	Δ
commonsenseqa	1,221	0.704	0.672	-0.032
gpqa_diamond	198	0.278	0.232	-0.045
kaleidoscope_ar	100	0.460	0.450	-0.010
kaleidoscope_bn	100	0.380	0.410	+0.030
kaleidoscope_de	100	0.520	0.560	+0.040
kaleidoscope_en	100	0.500	0.470	-0.030
kaleidoscope_es	100	0.520	0.570	+0.050
kaleidoscope_fa	100	0.280	0.290	+0.010
kaleidoscope_fr	100	0.230	0.290	+0.060
kaleidoscope_hi	100	0.290	0.300	+0.010
kaleidoscope_hr	100	0.270	0.250	-0.020
kaleidoscope_hu	100	0.320	0.260	-0.060
kaleidoscope_lt	100	0.550	0.570	+0.020
kaleidoscope_nl	100	0.360	0.410	+0.050
kaleidoscope_pt	100	0.690	0.730	+0.040
kaleidoscope_ru	100	0.230	0.330	+0.100

Source	Count	Gemma	MedGemma	Δ
kaleidoscope_sr	100	0.250	0.230	-0.020
kaleidoscope_uk	100	0.350	0.380	+0.030
mmlu_pro_biology	250	0.596	0.580	-0.016
mmlu_pro_business	250	0.252	0.248	-0.004
mmlu_pro_chemistry	250	0.184	0.172	-0.012
mmlu_pro_computer_science	250	0.304	0.272	-0.032
mmlu_pro_economics	250	0.472	0.452	-0.020
mmlu_pro_engineering	250	0.240	0.228	-0.012
mmlu_pro_health	250	0.352	0.412	+0.060
mmlu_pro_history	250	0.364	0.372	+0.008
mmlu_pro_law	250	0.240	0.232	-0.008
mmlu_pro_math	250	0.172	0.144	-0.028
mmlu_pro_other	250	0.308	0.260	-0.048
mmlu_pro_philosophy	250	0.276	0.352	+0.076
mmlu_pro_physics	250	0.152	0.184	+0.032
mmlu_pro_psychology	250	0.452	0.484	+0.032
truthfulqa_mc1	806	0.465	0.557	+0.092

Table 10: Exact full non-clinical source composition and endpoint movements.

Source	Count	Gemma	MedGemma	Δ
kaleidoscope_hu	100	0.320	0.260	-0.060
mmlu_pro_other	250	0.308	0.260	-0.048
gpqa_diamond	198	0.278	0.232	-0.045
mmlu_pro_computer_science	250	0.304	0.272	-0.032
commonsenseqa	1,221	0.704	0.672	-0.032
kaleidoscope_en	100	0.500	0.470	-0.030
mmlu_pro_math	250	0.172	0.144	-0.028
kaleidoscope_hr	100	0.270	0.250	-0.020

(a) Selected regressions

Source	Count	Gemma	MedGemma	Δ
kaleidoscope_ru	100	0.230	0.330	+0.100
truthfulqa_mc1	806	0.465	0.557	+0.092
mmlu_pro_philosophy	250	0.276	0.352	+0.076
mmlu_pro_health	250	0.352	0.412	+0.060
kaleidoscope_fr	100	0.230	0.290	+0.060
kaleidoscope_nl	100	0.360	0.410	+0.050
kaleidoscope_es	100	0.520	0.570	+0.050
kaleidoscope_de	100	0.520	0.560	+0.040
kaleidoscope_pt	100	0.690	0.730	+0.040
mmlu_pro_physics	250	0.152	0.184	+0.032
mmlu_pro_psychology	250	0.452	0.484	+0.032
kaleidoscope_uk	100	0.350	0.380	+0.030
kaleidoscope_bn	100	0.380	0.410	+0.030

(b) Selected gains

Table 11: Endpoint-selected diagnostic slices. Selection uses source-level endpoint gaps of at least 0.02 accuracy and at least 80 examples.

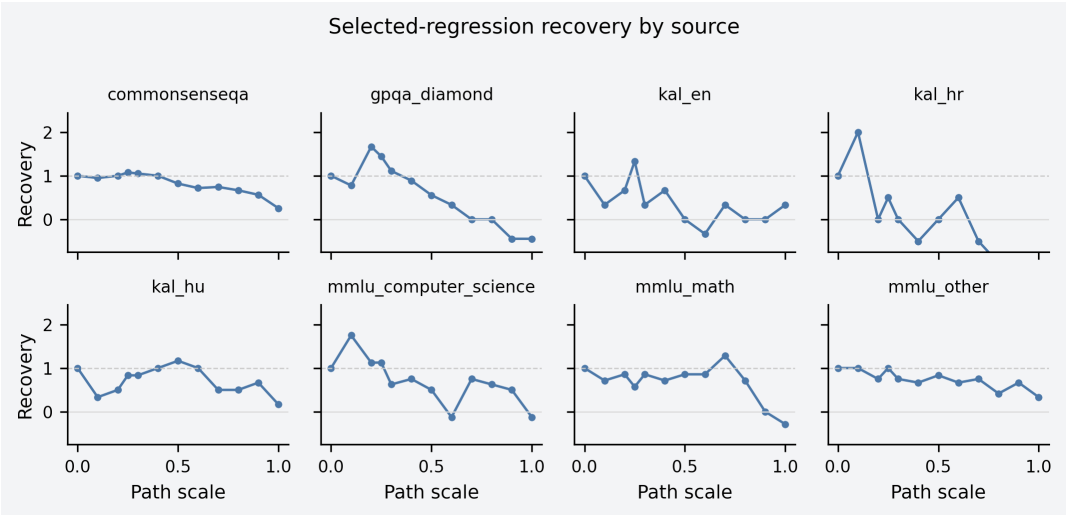

(a) Selected-regression recovery

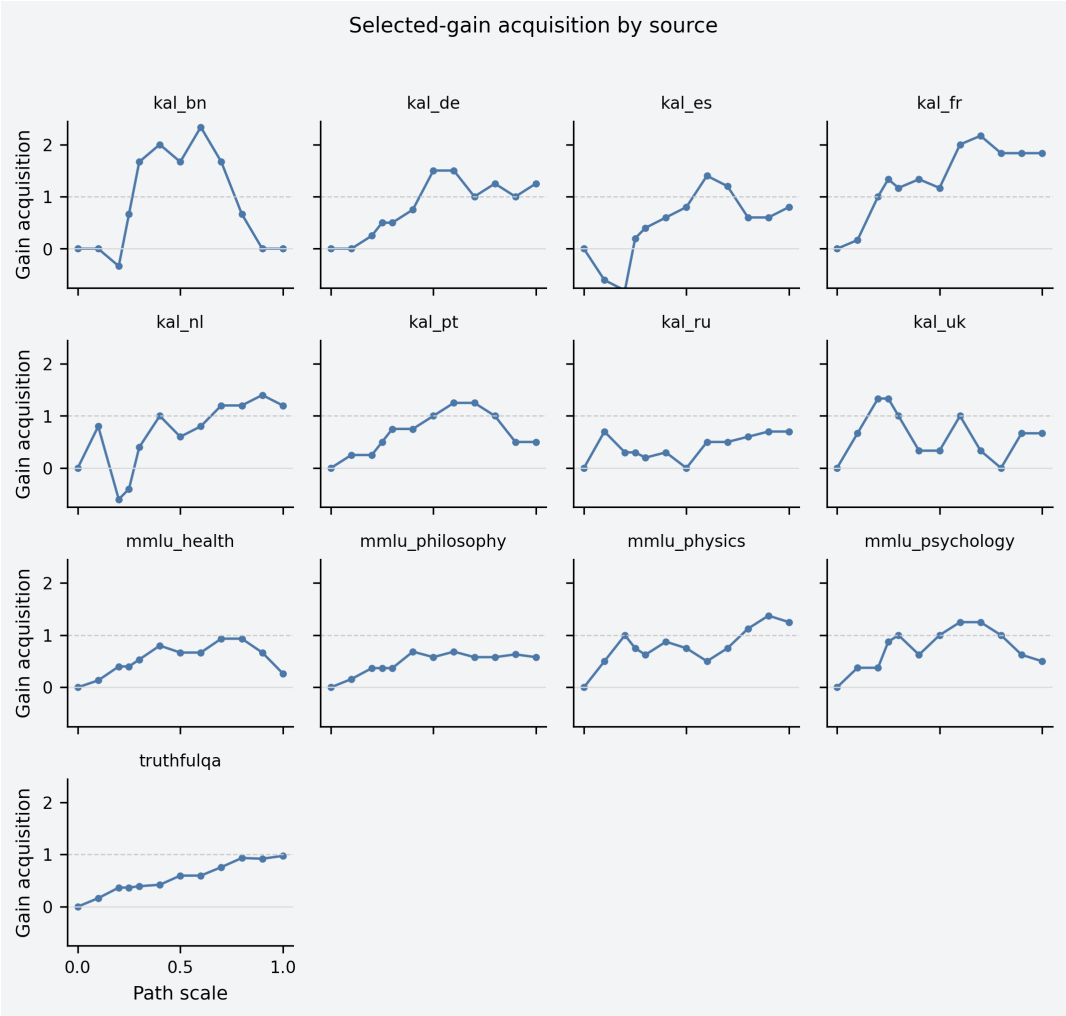

(b) Selected-gain acquisition

Figure 8: Per-source selected-slice diagnostics along the full decoder-side path. These views are conditional on endpoint slice selection and are used as diagnostics rather than broad non-clinical estimates.

Target	Control	n	Med. retention	Reg. recovery	Structured
Attention+down	delta-energy	10	0.416±0.151	0.431±0.136	0.510/0.570
Attention+down	matrix-count	10	0.703±0.112	0.388±0.159	0.510/0.570
Attention+down	parameter-count	10	0.417±0.086	0.585±0.166	0.510/0.570
MLP	delta-energy	10	0.563±0.100	0.262±0.242	0.699/0.279
MLP	matrix-count	10	0.437±0.077	0.513±0.224	0.699/0.279
MLP	parameter-count	10	0.814±0.067	0.236±0.175	0.699/0.279

Table 15: Matched random controls over 10 seeded draws. Entries report mean ± standard deviation; the final column gives the corresponding structured-bucket medical retention / selected-regression recovery, with both controls and structured comparators evaluated at $t = 1$.

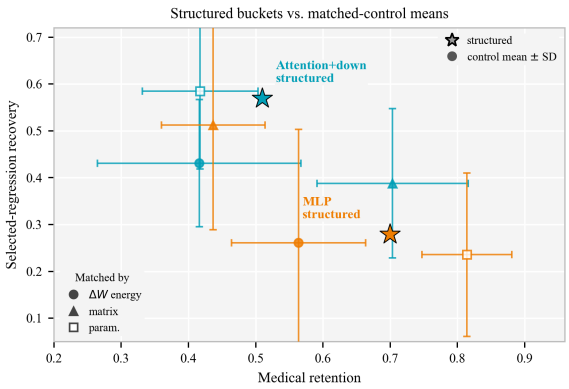

Figure 9: Matched random buckets approach the structured component buckets. Stars denote the structured MLP and attention+down_proj buckets; other markers are 10-seed random-control means, with one-standard-deviation bars, matched by parameter count, matrix count, or ΔW energy. Because several controls approach the stars, the plot supports partial sufficiency rather than unique component-family localization.

Rolled-back family	α	Med. ret.	Reg. rec.
Attention	0.00	0.699	0.279
Attention	0.25	0.784	0.419
Attention	0.50	0.902	0.314
Attention	0.75	0.993	0.256
Attention	1.00	0.974	0.070
MLP	0.00	0.359	0.593
MLP	0.25	0.699	0.477
MLP	0.50	0.876	0.384
MLP	0.75	0.980	0.302
MLP	1.00	0.974	0.070

Table 16: Anchored rollback paths. Lower α rolls back the named family while leaving the rest of the decoder update fixed at the specialist endpoint.

A.4 Qwen2.5–HuatuoGPT-o1 Replication

The replication uses the same 1,810 medical and 7,325 non-clinical examples, scoring rule, normalized readouts, and bootstrap procedure. Its endpoint-conditioned regression and gain slices are selected within the pair. The 196 aligned decoder projection matrices contain approximately 6.53B non-embedding parameters.

Endpoint view	Estimate	95% CI	
Medical composite	+0.0453	+0.0254	+0.0641
Selected regressions	-0.0617	-0.0813	-0.0417
Selected gains	+0.0554	+0.0387	+0.0721

t	Med. acc.	Med. ret.	Reg. rec.	Gain acq.
0.00	0.6481	0.000	1.000	0.000
0.50	0.6873	0.866	0.789	0.824
0.60	0.6961	1.061	0.585	0.919
0.80	0.6972	1.085	0.458	1.103
1.00	0.7017	1.183	0.556	1.147

Table 17: Qwen–HuatuoGPT endpoint movements and evaluated full-path grid.

Group	Matrices	Param. share	ΔW energy	Mean rank
Attention	112	12.6%	12.2%	477.7
MLP	84	87.4%	87.8%	1522.3
gate_proj	28	29.1%	30.6%	1471
up_proj	28	29.1%	29.0%	1354
down_proj	28	29.1%	28.2%	1742

Table 18: Qwen decoder projection coverage and update geometry.

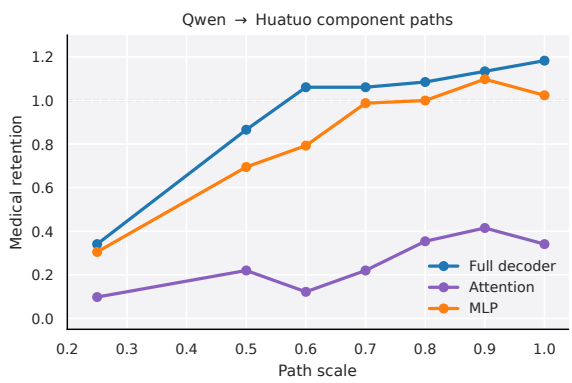

Figure 10: Qwen structured-family medical-retention trajectories at the evaluated path points. MLP is strongest, but its size motivates matched controls.

Target	Match	Med. mean	Range	Reg. mean	Gain mean
Attn+down	ΔW energy	0.660	0.573–0.780	0.744	0.674
Attn+down	Matrices	1.117	1.061–1.256	0.685	0.941
Attn+down	Parameters	0.667	0.476–0.817	0.799	0.707
MLP	ΔW energy	1.098	1.037–1.159	0.548	1.102
MLP	Matrices	0.680	0.427–0.902	0.837	0.713
MLP	Parameters	1.115	1.024–1.195	0.527	1.082

Table 19: Qwen matched controls at $t = 1$ over 10 seeded draws. Ranges show the observed minimum and maximum, not standard deviations or confidence intervals.

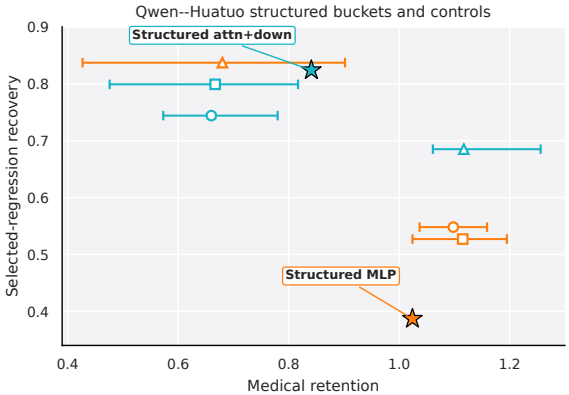

Figure 11: Qwen control means and observed ranges over 10 seeded draws. Stars mark the corresponding structured bucket at $t = 1$.

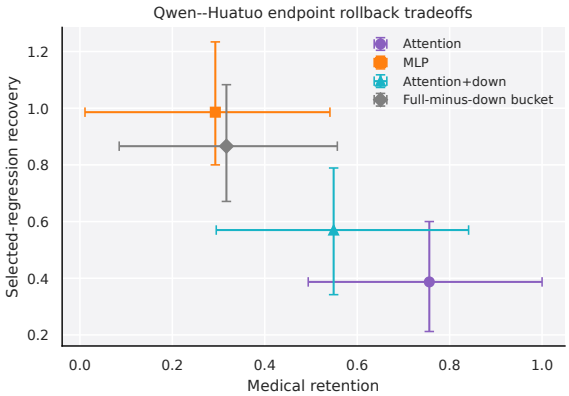

Figure 12: Qwen rollback tradeoff. No tested family simultaneously preserves the medical movement and fully recovers selected regressions.

A.5 MLP Neuron-Level Activation Diagnostic

As a secondary diagnostic, we ask whether the coarse component results hide a simpler pattern at the level of MLP intermediate neurons. We sample 64 examples from each of the medical, selected-regression, and selected-gain views and run both checkpoints on the same prompts. For each decoder layer, we capture the last-token MLP intermediate state $\mathrm{act}(\mathrm{gate_proj}(x)) \odot \mathrm{up_proj}(x)$, yielding arrays of shape $64 \times 34 \times 10240$ for each diagnostic group and checkpoint. We define drift as the mean absolute Gemma–MedGemma activation difference, and define a proxy importance score as the MedGemma activation magnitude multiplied by the corresponding $\mathrm{down_proj}$ column norm. These are descriptive proxies, not causal neuron ablations.

Table 22 reports top-k Jaccard overlaps between the resulting neuron rankings. The main pattern is conservative: high-importance neurons are strongly shared across medical, selected-regression, and selected-gain groups, whereas importance and specialization drift overlap only partially. Drift rankings are more similar across medical and regression groups than either drift ranking is to medical importance. Layer summaries show the same separation: mean drift is strongest in late layers, while proxy importance includes layer 33 but also earlier and middle layers. Thus this finer-grained diagnostic does not overturn the main localization result; it supports the view that the specialization update is structured but not cleanly explained by a small medical-specific neuron set.

Ranking comparison	Top-100	Top-1k	Top-5k
Medical imp. vs medical drift	0.212	0.255	0.275
Medical imp. vs regression drift	0.250	0.277	0.283
Medical imp. vs regression imp.	0.786	0.619	0.603
Medical drift vs regression drift	0.515	0.514	0.520
Regression imp. vs regression drift	0.266	0.278	0.317
Medical imp. vs gain imp.	0.802	0.630	0.618
Regression imp. vs gain imp.	0.852	0.812	0.797

Table 22: Top-k Jaccard overlaps for the MLP neuron diagnostic. "Imp." denotes the down-projection-weighted activation-magnitude proxy. The diagnostic uses 64 examples per group and is reported only as descriptive support for the coarse localization analysis.

A.6 Additional Descriptive ΔW Tables and Figures

The main text includes the decoder-side relative-change heatmap and layerwise RMS curve. Here we report additional descriptive ΔW diagnostics used to design the bucket set, including spectral energy and effective-rank views. These are not separate intervention results.

Module-only path	Med. retention
down_proj	0.512
up_proj	0.439
gate_proj	0.366
o_proj	0.183
v_proj	0.061
q_proj	0.012
k_proj	-0.037

Leave-one-module-out path	Med. retention
Full minus up_proj	1.183
Full minus down_proj	1.159
Full minus q_proj	1.146
Full minus gate_proj	1.146
Full minus v_proj	1.110
Full minus k_proj	1.098
Full minus o_proj	1.085

Table 20: Qwen module-only and leave-one-module-out paths at $t = 1$.

Full rollback	Med. retention	Reg. recovery	Gain acquisition
Attention	0.756 [0.494, 1.000]	0.387 [0.212, 0.600]	0.882 [0.723, 1.084]
MLP	0.293 [0.011, 0.541]	0.986 [0.800, 1.234]	0.471 [0.297, 0.677]
Attn+down	0.549 [0.295, 0.841]	0.570 [0.342, 0.789]	1.000 [0.790, 1.296]
Full-minus-down	0.317 [0.085, 0.557]	0.866 [0.671, 1.083]	0.559 [0.394, 0.774]

Table 21: Qwen full rollback results with 95% bootstrap intervals.

Module	Family	All n	All rel.	All top-32	All eff. rank	Dec. rel.	Dec. top-32
q_proj	attention	61	2.486	0.178	786.8	0.368	0.137
v_proj	attention	61	2.121	0.136	668.4	0.338	0.104
k_proj	attention	61	1.941	0.174	611.8	0.373	0.142
down_proj	MLP	34	0.370	0.039	2171.0	0.370	0.039
o_proj	attention	34	0.337	0.122	1086.6	0.337	0.122
gate_proj	MLP	34	0.261	0.033	2175.5	0.261	0.033
up_proj	MLP	34	0.243	0.034	2168.4	0.243	0.034

Table 23: Module-level ΔW summaries. "All" aggregates all selected aligned matrices, including the vision tower where applicable. "Dec." recomputes the same relative-change and mean top-32 energy summaries over decoder-side matrices only. Relative change is computed as the aggregate Frobenius norm of ΔW divided by the corresponding aggregate base-model norm.

Layer	Rel. change	RMS	Attn rel.	MLP rel.	Attn/MLP	Eff. rank	Max module
19	1.286	0.0222	2.649	0.248	5.81	1208.2	v_proj
26	1.283	0.0215	2.463	0.247	5.97	1173.2	v_proj
2	1.254	0.0219	2.375	0.255	5.67	1049.2	q_proj
20	1.241	0.0216	2.193	0.262	5.62	1196.8	v_proj
18	1.239	0.0219	2.510	0.248	5.62	1212.1	v_proj
17	1.239	0.0214	2.438	0.256	5.50	1160.1	v_proj
21	1.203	0.0215	2.215	0.251	5.57	1225.7	v_proj
22	1.198	0.0212	2.311	0.240	5.70	1235.9	v_proj

Table 24: Top decoder-side layers by layer-level relative change. The attention/MLP ratio compares Frobenius norms of the attention and feed-forward parts of each layer's ΔW.

Layer	Module	Rel. change	RMS	Top-32 energy	Eff. rank	k_{80}
27	k_proj	0.854	0.0173	0.165	665.4	476
7	k_proj	0.843	0.0176	0.152	673.8	455
27	v_proj	0.837	0.0170	0.084	822.9	548
11	down_proj	0.830	0.0044	0.053	2070.3	1441
19	o_proj	0.825	0.0083	0.114	1073.8	734
7	v_proj	0.814	0.0170	0.099	771.4	508
15	down_proj	0.797	0.0042	0.046	2119.2	1461
8	k_proj	0.767	0.0167	0.180	632.7	439
18	o_proj	0.765	0.0083	0.128	1052.7	738
8	v_proj	0.729	0.0159	0.093	790.1	522

Table 25: Top decoder-side matrices by matrix-level relative change. k_{80} is the number of singular directions needed to explain 80% of the matrix ΔW energy.

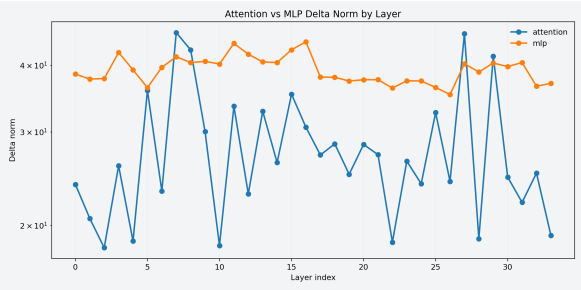

(a) Attention vs MLP delta by layer

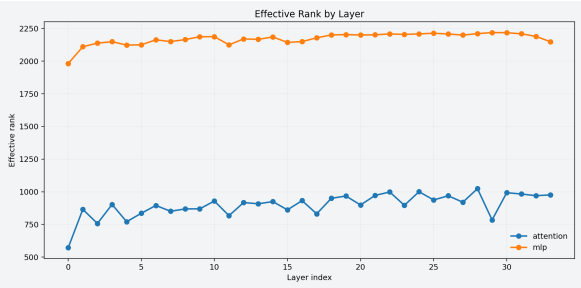

(b) Effective rank by layer

Figure 13: Additional decoder-side layer diagnostics. These views show that the decoder-side update is depth-structured, while the intervention analysis in the main text focuses on component-level bucket sufficiency.

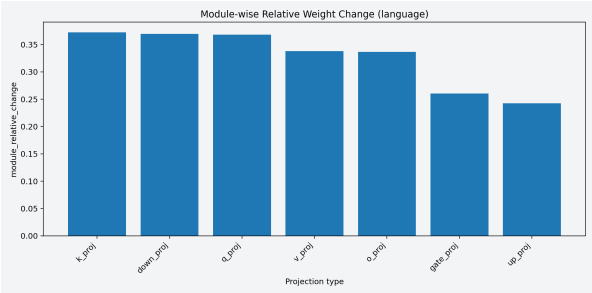

(a) Module relative change

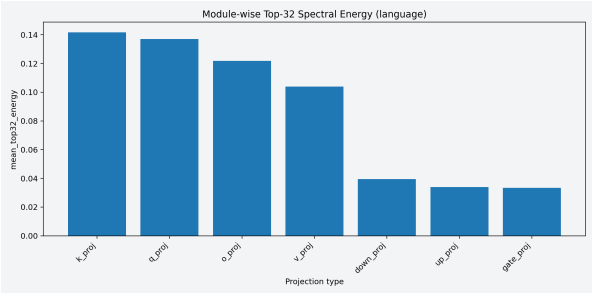

(b) Module top-32 energy

Figure 14: Decoder-side module diagnostics complementing Table 23.

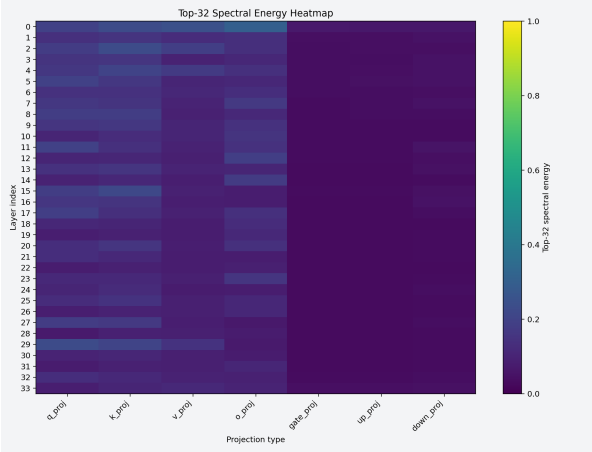

(a) Top-32 energy heatmap

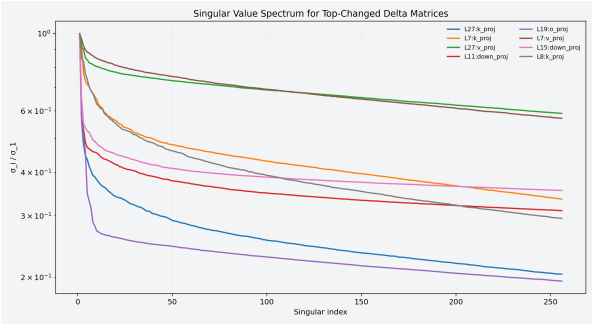

(b) Singular-value spectra

Figure 15: Additional spectral diagnostics for decoder-side ΔW matrices.

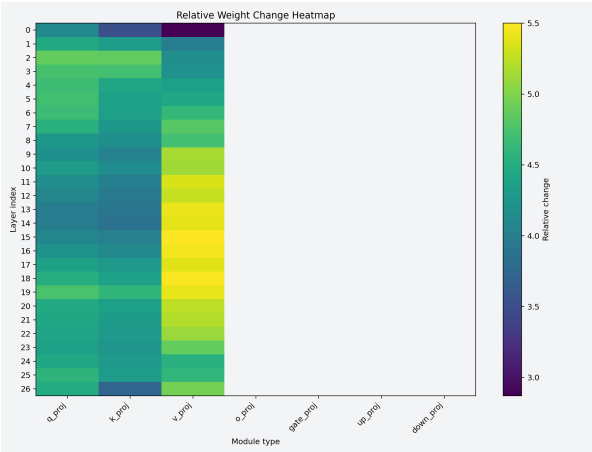

(a) Vision relative-change heatmap

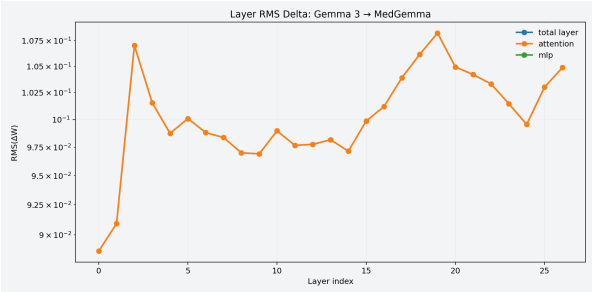

(b) Vision layer RMS delta

Figure 16: Vision-side descriptive ΔW context. These plots explain why the global raw ΔW screen contains large vision-tower changes, even though the main intervention analysis targets the decoder backbone for text-only medical evaluation.